Electronic Supplementary Information (ESI)

Transformation of Amorphous Calcium Phosphate to Monoclinic Nano-hydroxylapatite

Yao Yan,[abc] Yanan Fang,[d] Jun Li,[abc] Yongqiang Yang,[ab] Fanrong Chen,[ab] Shijun Wu,[*ab] Thomas Hooper,[d] Ankit Jaiswal[d] and Tim White[*d]

[a]CAS Key Laboratory of Mineralogy and Metallogeny & Guangdong Provincial Key Laboratory of Mineral Physics and Materials, Guangzhou Institute of Geochemistry, Chinese Academy of Sciences, 511 Kehua Street, 510640 Guangzhou, China.

[b]CAS Center for Excellence in Deep Earth Science, 511 Kehua Street, 510640 Guangzhou, China.

[c]University of Chinese Academy of Sciences, 19 Yuquan Road, 100049 Beijing, China.

[d]School of Materials Science & Engineering, Nanyang Technological University, 50 Nanyang Avenue, 639798 Singapore.

Corresponding Authors

*(S.W.) E-mail: wus@gig.ac.cn, Tel.: +86-20-85290143.

*(T.W.) E-mail: tjwhite@ntu.edu.sg, Tel.: +65-67904586.

1. Supplementary Experimental

1.1 Sample Preparation

Ammonium dihydrogen phosphate ($NH_4H_2PO_4$), calcium nitrate tetrahydrate ($Ca(NO_3)_2 \cdot 4H_2O$), 25-28 wt% ammonia solution ($NH_3 \cdot H_2O$), and absolute ethanol from Sigma–Aldrich were used for the synthesis without further purification. $Ca(NO_3)_2 \cdot 4H_2O$ and $NH_4H_2PO_4$, which served as Ca and P sources, were dissolved in 250 mL ultra-pure water separately, followed by a prescribed mass of $NH_3 \cdot H_2O$. Subsequently, the two solutions were quickly mixed, sealed in a reaction flask, placed in a constant temperature cabinet (25°C), and magnetically stirred (600 rpm). The initial ion concentrations and $NH_3 \cdot H_2O$ content are collated in Table S1, together with the supersaturation of the HAp solutions ($\log_e S_{HAp} = \ln S_{HAp}$) after mixing.

Over 24 hours, the mother solutions and the solid-liquid mixtures were separated at intervals. The liquid samples were diluted immediately to avoid precipitation before analysis of Ca and P using ICP-OES. The solid products were twice dispersed in 50 mL of 50% ethanol-50% deionized water (wt%) with the solid separated by centrifugation (5,000 rpm). Finally, the solids were washed in distilled water, and the suspensions were centrifuged and vacuum freeze-dried (-58℃; 20 mbar partial vacuum) for 24 h. These dried precipitates were stored at -80℃ to prevent phase transformation; our storing temperature is much lower than the regular freezer[1, 2]. The name of each solid has a suffix to imply its sampling time, e.g., 0.5ACP-15s indicated the sample collected 15 s after the reaction in the system 0.5ACP.

Table S1. Initial ion concentrations, $NH_3 \cdot H_2O$ content, and $\ln S_{HAp}$ for αACP synthesis

Sample Number	Ca sources		P sources		$\ln S_{HAp}$
	Ca^{2+}	$NH_3 \cdot H_2O$	PO_4^{3-}	$NH_3 \cdot H_2O$	

(αACP)	M (mol/L)	m (g)	M (mol/L)	m (g)	
0.01ACP	0.005	0.3	0.002	0.04	19.25
0.025ACP	0.01	0.75	0.004	0.1	21.12
0.05ACP	0.025	1.5	0.01	0.2	22.40
0.1ACP	0.05	3	0.02	0.4	23.67
0.25ACP	0.1	7.5	0.04	1	25.42
0.5ACP	0.25	15	0.1	2	26.84
1ACP	0.5	30	0.2	4	28.36

The initial Ca/P molar ratio in the mother solution was fixed at 2.5 for all experiments, as Kim et al.[3] noted, more excess calcium ions in the solution, and the Ca/P molar ratio of the final precipitates will be closer to the stoichiometric value of 1.67. The opening concentration of the Ca solution (based on the system before mixing) was recorded as α mol/L such that αACP-*t* represents the product sampled at time *t* (*t*=15s-24h). All experiments were performed in triplicate. Solution pH was continuously monitored, and the standard deviation (Stdev) of pH at each time point was <0.02.

1.2 Phase Characterization

The phase assemblage of the vacuum freeze-dried samples was analyzed by powder X-ray diffraction (XRD) using a Bruker D8 Advance diffractometer (Bruker AXS, Germany). Data were accumulated using Cu Kα radiation (40 kV/40 mA) over the scanning range of 5-120º (2θ) with a step speed of 2º (2θ)/min. For quantitative phase analysis, Rietveld refinements were undertaken with TOPAS Version 3 (Bruker AXS, America) for the crystalline αACP-24h with Fundamental Parameters (FP) used for the peak asymmetry correction. The ratio of amorphous phases and crystalline contents in solid samples was analyzed by including an internal standard

of silica powder (wt%=10%) manually ground in the samples. The reference lattice parameters were: (i) $P6_3/m$: ICSD 26204, a=b=9.424Å, c=6.879Å; (ii) $P112_1/b$: ICSD 34457, a= 9.4214 Å, b= 18.8428 Å, c= 6.8814 Å; and (iii) $P\bar{1}$: ICSD 172997, a=9.6987Å, b=9.6933Å, c=7.0170Å.

1.3 Electron Microscope Observation

The morphology and lattice perfection of the nanoparticles was observed by a field emission transmission electron microscope (TEM; FEI Talos F200s, America) and high-resolution TEM (HRTEM; JEOL 2100F, Japan) complemented by energy-dispersive X-ray spectroscopy (EDS, Apollo X-SDD Det, America) to investigate elemental composition. The TEM specimens were prepared by ultrasonically dispersing a small quantity of the solid in absolute ethanol solution for 10 minutes, placing drops of the supernatant on ultra-thin carbon films of 300 mesh, and allowing the ethanol to evaporate entirely at room temperature. The samples were observed at a voltage of 200 kV, spot size 6, with a beam current under 1 nA. Fast-focusing and shorter exposure times were used to minimize electron beam-induced damage. The FFT image of $P6_3/m$ and $P112_1/b$ was generated by Java electron microscopy simulation (JEMS) software.

1.4 Spectroscopy Characterization

Fourier-transform infrared (FT-IR) spectra were collected at room temperature with a Bruker 142 Vertex-70 instrument using the KBr pellet method between 4000 cm^{-1} and 400 cm^{-1} wavenumbers at a resolution of 2 cm^{-1}. Nuclear Magnetic Resonance (NMR) spectra were acquired for ^{31}P with a wide bore solid-state nuclear magnetic resonance spectrometer (Bruker Advance III WB300, Germany) at a MAS frequency using a cross-polarization magic angle spinning (CPMAS) pulse sequence. A contact period of 5000 μs was implemented, a relaxation delay of 5 s was used, and 512 scans were performed. Spectra were indirectly referenced against tetramethylsilane (TMS). A high-resolution confocal laser Raman spectrometer (WITec

alpha300R, Germany) was adopted to conduct an accurate evaluation of ACP transformation progression and crystallinity as a function of transformation time and initial ion concentrations (Table S1). No smoothing and intensity normalization was adopted for Raman data treatment, and its peak identification and fitting were performed with Gaussian functions focused on the ν_1 band. Further data treatment for the peak position and FWHM from ca. 950-960 cm^{-1} was performed piecewise using curve fitting software.

1.5 Elemental Concentration Measurements

The chemical compositions (Ca and P) of solids and liquids were analyzed by an inductively coupled plasma optical emission spectrometer (ICP-OES; Varian Vista PRO, Australia). To avoid precipitation, the solutions were diluted immediately after sampling with nitric acid (3 vol%). The solid samples were dissolved and diluted by nitric acid (3% vol%). Both liquid and solid samples were further diluted to meet the optimal instrumental test accuracy.

1.6 pH and SSA Measurements

The pH was monitored during the ACP transformation process by a Sartorius PB-10 pH meter. Approximately 0.1 g of sample was used for specific surface area (SSA) measurements by N_2 (P/Po = 0.3) adsorption (Micromeritics Instruments ASAP 2460, America) at room temperature.

1.7 Wet Chemistry Calculation

The solution supersaturations with respect to HAp (S_{HAp}) were determined using VMINTEQ 3.0 with the activity coefficients calculated using the Debye–Hückel equation (parameter b = 0.3, Formula S1). The solubility product (pK_{sp}) of HAp (pK_{sp}=58.33, MINTEQ database: NIST 46.7) was adopted in the wet chemistry calculation, where {X} represents the activity of species X.

$$S_{HAp} = \frac{\{Ca^{2+}\}^5\{PO_4^{3-}\}^3\{OH^-\}}{K_{sp,HAp}} \quad \textbf{(Formula S1)}$$

2. Supplementary Results

2.1 Formation of ACP

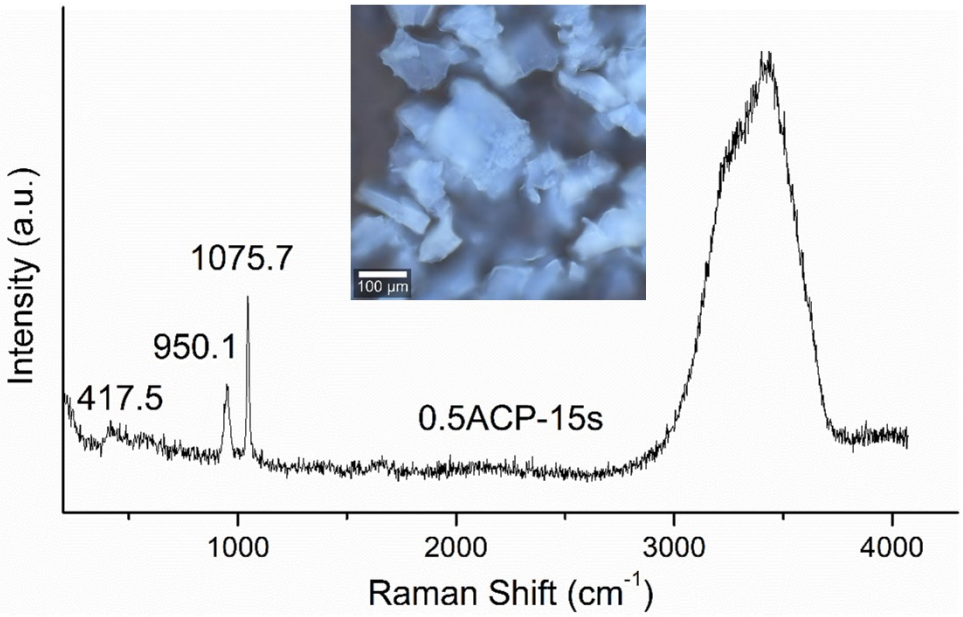

Figure S1. Raman spectrum and inserted scanning secondary electron image (SEI) of freeze-dried 0.5ACP-15s.

When Ca and P sources were combined, a white emulsion formed instantly. αACP-15s was collected for morphological examination and phase analysis. As a tetrahedral anion, the PO_4^{3-} could be subdivided into four normal Raman-active vibrations: ν_1 arises from symmetrical P-O stretching; ν_2 is the O-P-O angle scissors motion; ν_3 reflects antisymmetric P-O stretching, and ν_4 is the O-P-O bending.[4, 5] Previously, the transformation of ACP to HAp was characterized by shifts of the phosphate group ν_1 symmetrical stretching band, from a broad peak at 950 cm^{-1} to a sharp peak at 960 cm^{-1}.[4, 5] Sample αACP-15s showed a strong band at ca. 950 cm^{-1}, suggesting that ACP formed immediately upon calcium and phosphorus source mixing. Other Raman-active

phosphate vibrational bands occurred at 1075.7 (ν_3) and 417.5 cm^{-1} (ν_2)[5, 6] (Figure S1). It is noteworthy that a weak carbonate band would appear at ca. 1070 cm^{-1} convoluting with the low-intensity ν_3 phosphate band.[7]

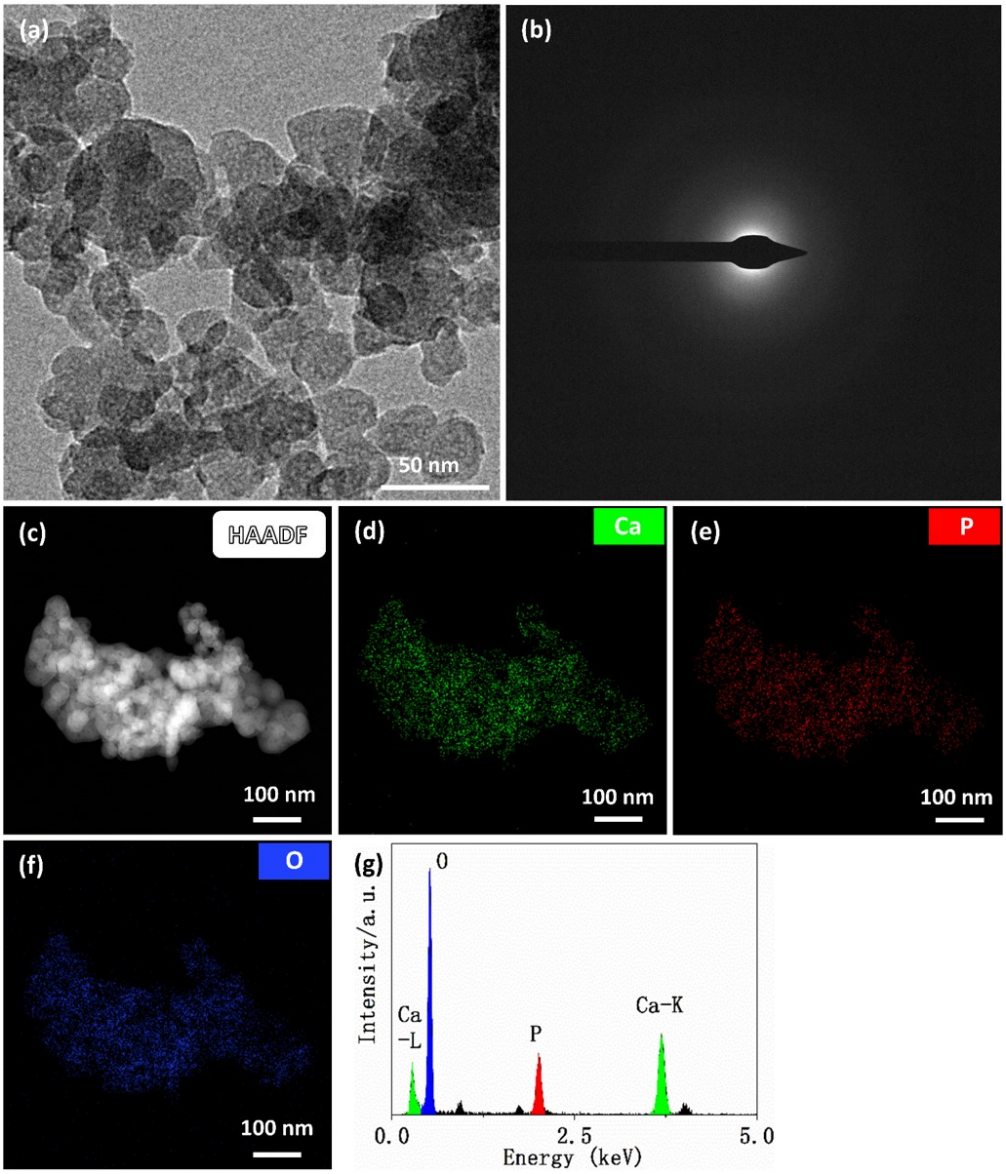

Figure S2. (a) The bright-field (BF) TEM image, (b) selected area electron diffraction (SAED) pattern, (c-f) elemental mapping image and (g) energy dispersive X-ray spectroscopy (EDX) of 0.5ACP-15s.

The 0.5ACP-15s (designated ACP1) morphology was as nano-sized spherical aggregates with diameters of less than 50 nm (Figure S2a) that were amorphous (Figure S2b) and anhedral, consistent with limited crystallinity as previously reported.[8] By contrast, the initially precipitated non-crystalline phase (ACP2) was floccular.[9] The elemental maps (Figure S2c-f) and EDX spectrum (Figure S2g) showed that Ca, P, and O were homogeneous.

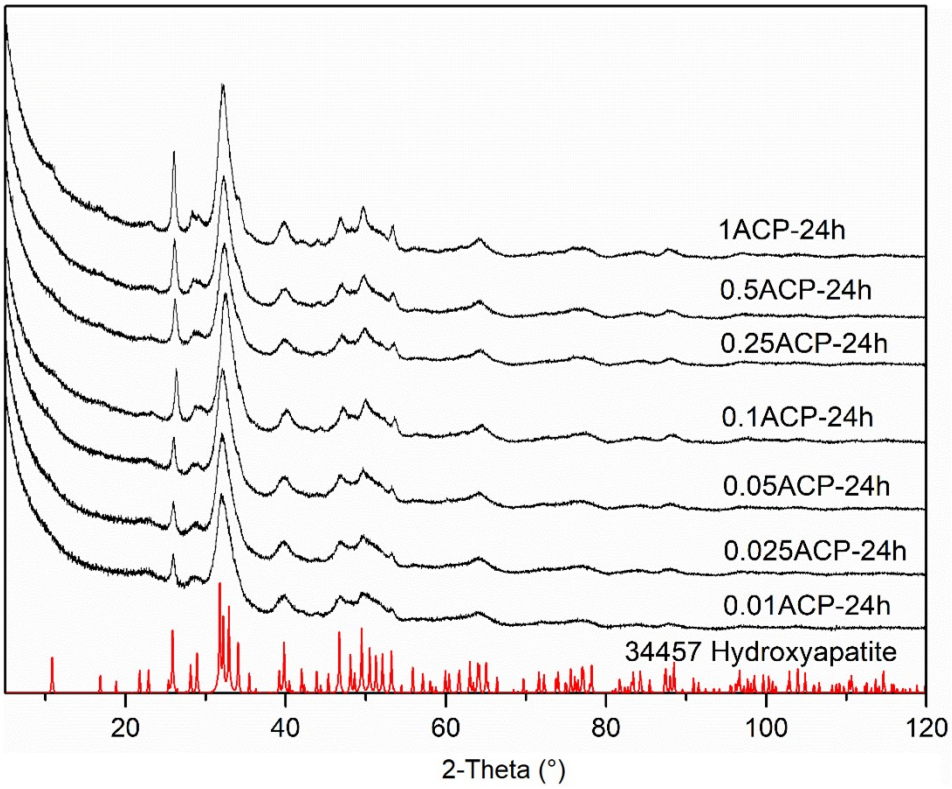

Figure S3. Measured X-ray-diffraction spectrums of (0.01-1)ACP-24h crystalline samples and standard hydroxyapatite (ICSD-34457) XRD image for peak comparison.

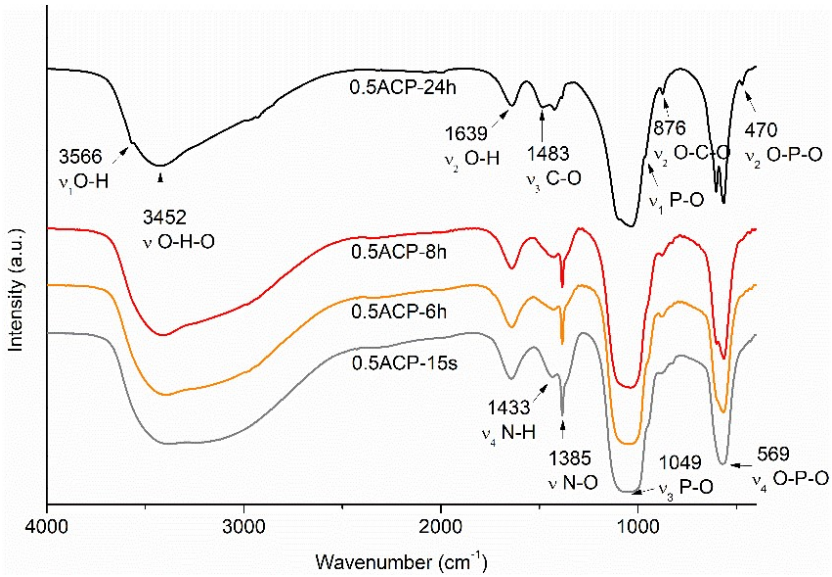

Figure S4. Fourier transformed-infrared (FT-IR) of 0.5ACP at different transformation times.

FT-IR spectra of non-crystalline calcium phosphate (0.5ACP-15s), poorly crystalline HAp (0.5ACP-8h and 0.5ACP-9h), and well crystalline HAp (0.5ACP-24h) all contain a broad and strong -OH stretching vibration at ca. 3452 cm^{-1} together with a band at 1639 cm^{-1} (Figure S4), typical of the stretching vibration of adsorbed or bound water[10] plus a hydroxyl group vibration at 3566 cm^{-1}.[11] Better crystalline 0.5HAp showed a narrower hydroxyl bandwidth and a decrease in water content. Features at 1385 and 1433 cm^{-1} are attributed to the stretching modes of NO_3^- and NH_4^+, respectively. There is evidence that NO_3^- could occupy the sites of PO_4^{3-},[12] and is released with increasing ACP crystallinity. CO_3^{2-} absorption peaks at 1483 cm^{-1} and 876 cm^{-1} were attributable to CO_2 uptake from the air. These two peaks are consistent with 0.5ACP-12h existing as a B-type HAp, where CO_3^{2-} displaces PO_4^{3-} in the T position rather than the hydroxyls (A-type). B-type HAps typically appear in powders precipitated from aqueous solutions under vigorous mixing at room temperature,[13-15] and are supposed similar to bioapatite.[13] CO_3^{2-} incorporation could promote changes in cell parameters and reduced symmetry ($P112_1/b$) of ACP products.[15] The bands at 470, 1049, and 569 cm^{-1} were ν_2 (flexural vibration), ν_3 (stretching

vibration), and ν_4 (flexural vibration) absorption of PO_4^{3-}, respectively, with the weak ν_1 stretching vibration band masked by the ν_3 peak. The ν_4 vibration of 0.5ACP-24h split into 604 and 569 cm^{-1} bands, corroborating the XRD observation (Figure S3) of the crystalline state of 0.5ACP-24h.[2, 11] The reduced width of ν_3 suggests the chemical environment around P-O in amorphous structures is more intricate and varied than in crystals.[11, 13]

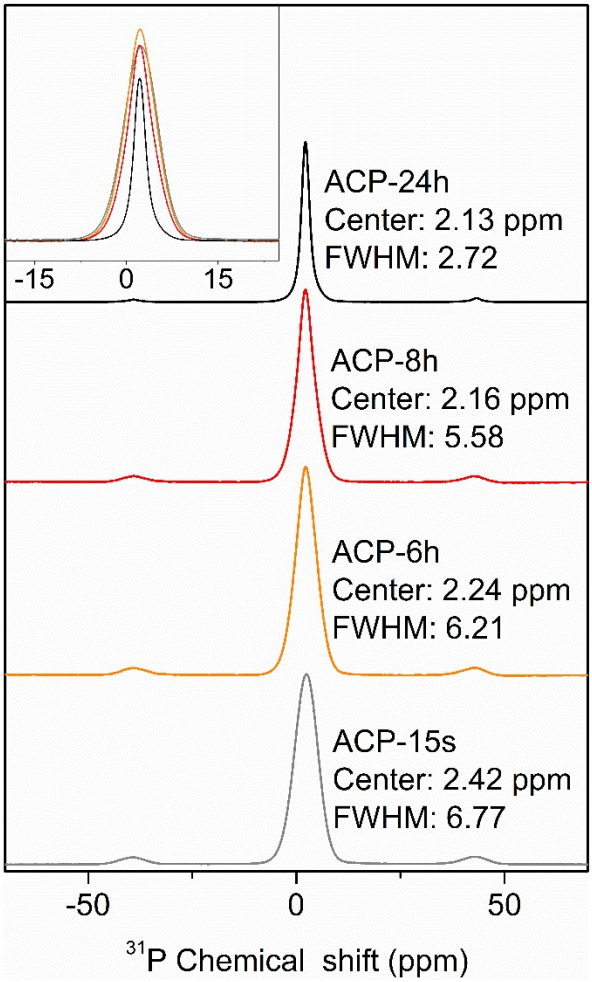

Figure S5. ^{31}P Solid-state NMR spectrum of 0.5ACP-*t*.

^{31}P nuclear magnetic resonance (NMR) spectroscopy is useful in studying phosphates due to its high sensitivity toward the ^{31}P isotope (100% natural abundance, I=1/2, and high receptivity).[17, 18] The ^{31}P NMR spectra of 0.5ACP-*t* showed a central band and two sidebands

(Figure S5) whose widths decreased with increasing crystallinity reflecting a more complex P environment in ACP.[17, 18] The sidebands of poorly crystalline ACP were stronger and broader, attributable to a small amount of protonated phosphate.[17] This phenomenon is expected by the Le Chatelier's principle, as precipitation of calcium phosphate removes PO_4^{3-} and moves the equilibrium of Formula S2 to the right.[19]

$$H_3PO_4 \rightleftharpoons H^+ + H_2PO_4^- \rightleftharpoons H^+ + HPO_4^{2-} \rightleftharpoons H^+ + PO_4^{3-} \quad \textbf{(Formula S2)}$$

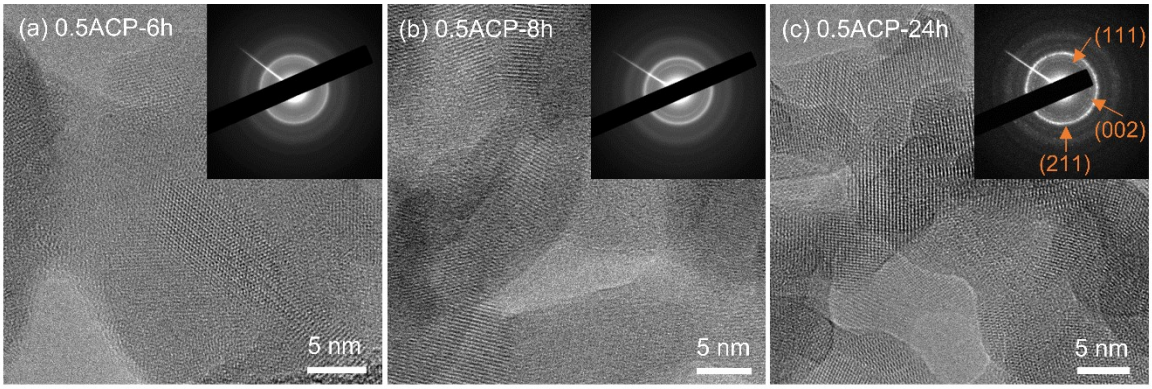

Figure S6. SAED patterns and low magnification TEM image of (a) 0.5ACP-6h, (b) 0.5ACP-8h, and (c) 0.5ACP-24h.

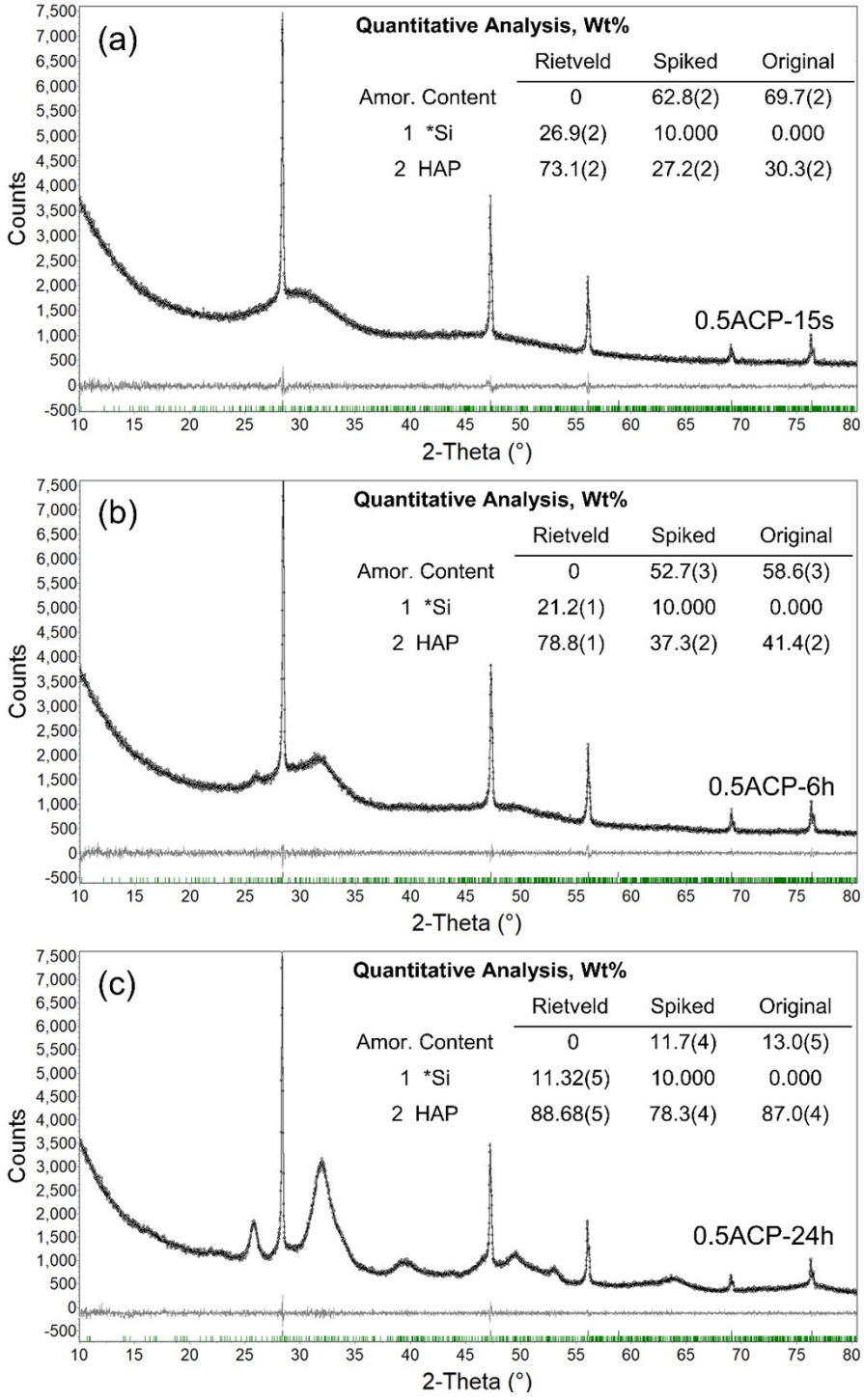

Figure S7. XRD quantitative analysis of amorphous content for (a) 0.5ACP-15s, (b) 0.5ACP-6h and (c) 0.5ACP-24h sample by Rietveld fitting.

XRD quantitative phase analysis with the addition of an internal standard (10% Si powder) for 0.5ACP-24h (Figure S7) determined a non-diffracting amorphous content of 13.0 wt% together with crystalline nHAp. Because Cu Kα X-rays penetrate relatively deeply, it was not possible to differentiate dispersed aperiodic material from an amorphous overlayer. Nonetheless, the amorphous content/layer thickness decreases with aging time.[9, 11]

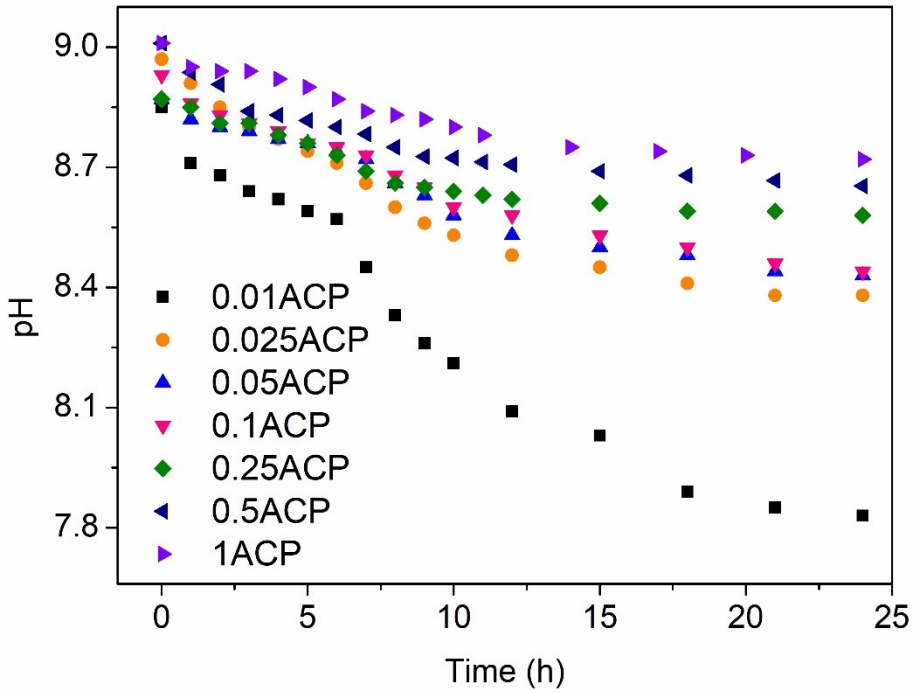

Figure S8. Time (t)-pH scatter patterns of αACP in mother solution.

Table S2. XRD refinement parameters for αACP-24h

αACP-24h	α=0.01	α=0.025	α=0.05	α=0.1	α=0.25	α=0.5	α=1
Space group	$P6_3/m$	$P6_3/m$	$P6_3/m$	$P6_3/m$	$P6_3/m$	$P6_3/m$	$P6_3/m$
a(Å)	9.41(4)	9.394(7)	9.426(1)	9.444(8)	9.414(8)	9.443(2)	9.436(8)
c(Å)	6.86(2)	6.8554	6.8797	6.891(5)	6.852(6)	6.8827(2)	6.869(5)
Volume (Å^3)	526(5)	524.0(8)	529.4(1)	532(1)	525(1)	531.6(2)	529(1)
R-Bragg	0.19	0.15	0.15	0.38	0.27	0.26	0.48
Space group	$P112_1/b$	$P112_1/b$	$P112_1/b$	$P112_1/b$	$P112_1/b$	$P112_1/b$	$P112_1/b$
a(Å)	9.30(9)	9.42(7)	9.43(3)	9.42(1)	9.44(3)	9.430(9)	9.41(8)
b(Å)	19.4(2)	19.0(1)	19.01(8)	18.97(3)	19.02(6)	18.99(2)	19.02(2)
c(Å)	6.86(5)	6.81(4)	6.82(2)	6.82(1)	6.84(2)	6.855(6)	6.90(4)
Volume (Å^3)	1052(18)	1039(14)	1041(7)	1038(3)	1046(6)	1046(2)	1058.9(6)
R-Bragg	0.10	0.13	0.12	0.15	0.16	0.15	0.12
Space group	$P\bar{1}$	$P\bar{1}$	$P\bar{1}$	$P\bar{1}$	$P\bar{1}$	$P\bar{1}$	$P\bar{1}$
a(Å)	9.6(1)	9.8(4)	9.85(7)	9.81(1)	9.96(5)	9.88(1)	9.80(2)
b(Å)	9.7(2)	9.4(3)	9.39(6)	9.59(2)	9.44(3)	9.64(2)	9.27(3)
c(Å)	6.88(7)	6.9(1)	6.85(3)	6.90(1)	6.94(3)	6.884(8)	6.91(2)
Volume (Å^3)	548(15)	552(34)	548(7)	546(2)	566(6)	553(2)	545(3)
R-Bragg	0.49	0.37	0.28	0.28	0.66	0.37	0.52

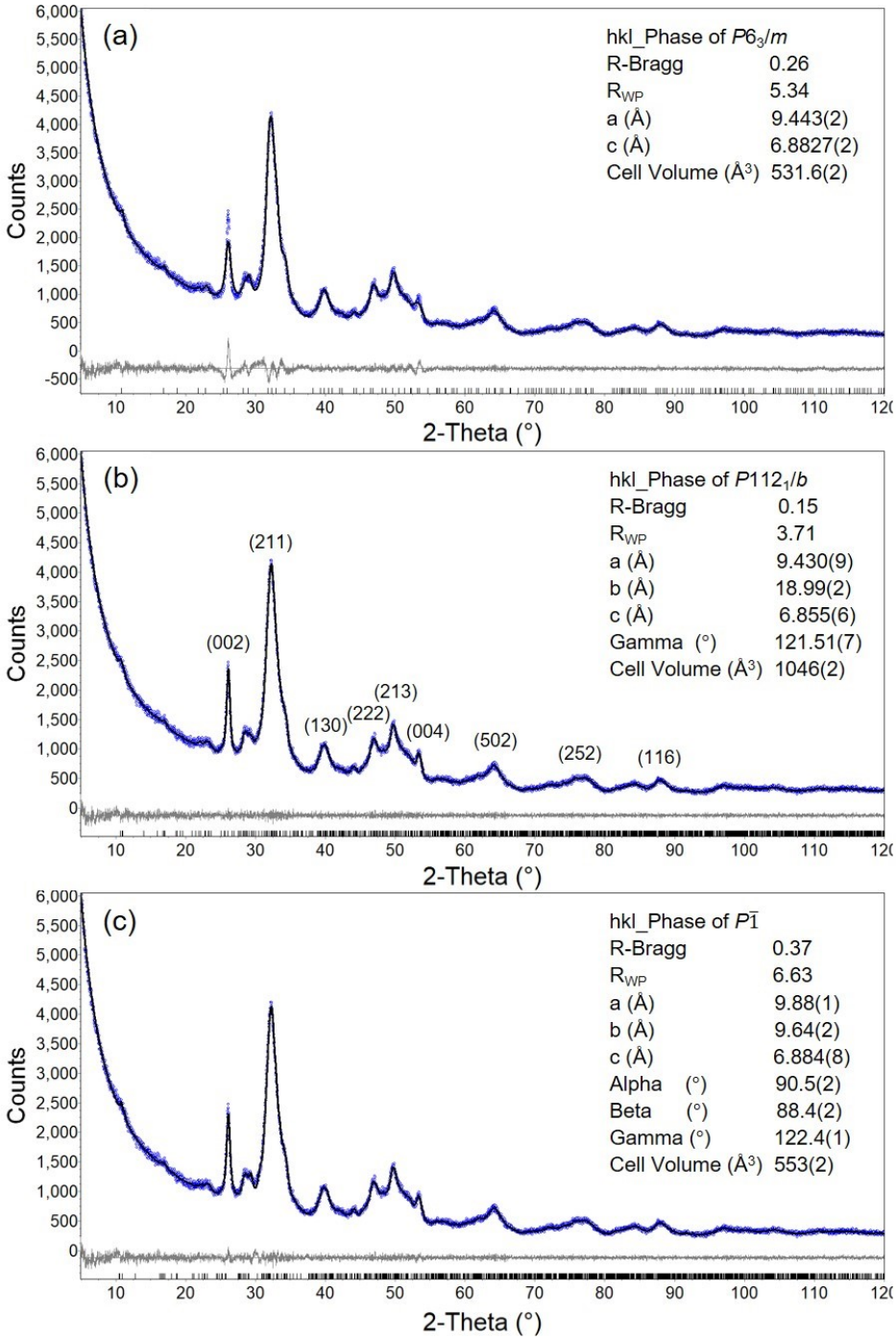

Figure S9. Measured X-ray-diffraction spectra (blue lines) of 0.5ACP-24h, and their Rietveld fitting pattern (black lines) compared with different hydroxylapatite structure (a) $P6_3/m$; (b) $P112_1/b$; (c) $P\bar{1}$, the differences between blue and black lines were reflected in the gray glitch lines.

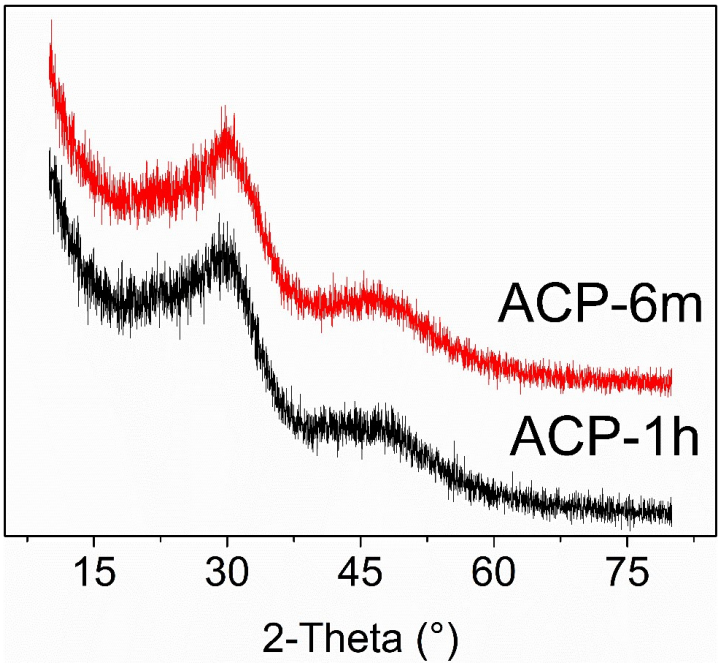

Figure S10. XRD patterns of dried 0.5ACP-1h and 0.5ACP-6m samples.

ACP is thermodynamically unstable, but can be preserved through storage in liquid nitrogen, refrigeration, or passivation by inorganic/organic stabilizers to prevent spontaneous crystallisation. Here, a vacuum freeze-dried 0.5ACP-1h sample (labeled as ACP-6m) was stable towards the air for up to 6 months and retained its amorphous character as confirmed by XRD (Figure S10). Dorozhkin[9] has suggested ACP may be stabilized through the crystallochemical incorporation of CO_3^{2-} carbonate ions, consistent with our FT-IR results (Figure S4).

Table S3. BET Specific Surface Area of selected apatite

Types of apatite	BET surface area (m^2/g)	Conditions	Reference
0.5ACP-15s	63.461±0.019	25°C, pH~9	This work
0.5ACP-6h	72.361±0.059	25°C, pH~9	This work
0.5ACP-8h	121.425±0.171	25°C, pH~9	This work
0.5ACP-12h	239.770±1.115	25°C, pH~9	This work
0.5ACP-24h	229.297±1.346	25°C, pH~9	This work
Bioapatite	1.2	-	[20]
Synthetic HAp	6.63	200 °C, pH 8.0	[21]
Copper doping HAp	77.5	200 °C, pH 8.0	[21]
Nano-HAp	137.14	25°C, pH 9.5	[22]
Nano-HAp	160	RT, pH 8.5	[23]
Nano-HAp	119	RT, pH11	[24]
High SSA ACP	154±9	22±2°C, pH 8	[25]
High SSA HAp	95±3	22±2°C, pH 8.8	[25]

As the specific surface area (SSA) of HAp correlates strongly with bioactivity,[26] this property is critical for in-vivo and in-vitro applications and is impacted by the rate of ACP crystallisation at ambient temperature. Here, the SSA increased gradually as ACP transformation proceeded, with a slight reduction as the crystals matured (Table S3). We assume the increased SSA may be caused by the irregular surface while ACP discharging water. The crystalline 0.5ACP-24h showed a superior SSA than referenced bioapatite, ionic doped HAp, nano-HAp, and high SSA ACP. The SSA of the crystalline precipitates (0.5ACP-24h, 229.29±1.346 m^2/g) was ca. 3.6 times its amorphous precursors (0.5ACP-15s, 63.461±0.019 m^2/g). Therefore the approach

presented in this work provides a convenient way to achieve high BET surface areas and non-impurity doped nano-HAp at room temperature.

REFERENCES

(1) Karimi, M.; Hesaraki, S.; Alizadeh, M.; Kazemzadeh, A., Synthesis of calcium phosphate nanoparticles in deep-eutectic choline chloride–urea medium: Investigating the role of synthesis temperature on phase characteristics and physical properties. *Ceram. Int.* **2016**, 42 (2), 2780-2788.

(2) Uskokovic, V.; Markovic, S.; Veselinovic, L.; Skapin, S.; Ignjatovic, N.; Uskokovic, D. P. Insights into the kinetics of thermally induced crystallization of amorphous calcium phosphate. *Phys. Chem. Chem. Phys*. **2018**, *20*, 29221-35.

(3) Kim, S.; Ryu, H. S.; Shin, H.; Jung, H. S.; Hong, K. S., In situ observation of hydroxyapatite nanocrystal formation from amorphous calcium phosphate in calcium-rich solutions. *Mater. Chem. Phys.* **2005**, 91 (2-3), 500-506.

(4) Combes, C.; Rey, C. Amorphous calcium phosphates: synthesis, properties and uses in biomaterials. *Acta Biomater.* **2010**, *6*, 3362-78.

(5) Song, H.; Liu, J.; Cheng, H. Structural and spectroscopic study of arsenate and vanadate incorporation into apatite group: Implications for semi-quantitative estimation of As and V contents in apatite. *Spectrochim. Acta A Mol. Biomol. Spectrosc.* **2018**, *188*, 488-94.

(6) Sauer, G. R.; Zunic, W. B.; Durig, J. R.; Wuthier, R. E. Fourier transform Raman spectroscopy of synthetic and biological calcium phosphates. *Calcif. Tissue Int.* **1994**, *54*, 414-20.

(7) Krajewski, A.; Mazzocchi, M.; Buldini, P. L.; Ravaglioli, A.; Tinti, A.; Taddei, P.; Fagnano, C. Synthesis of carbonated hydroxyapatites: efficiency of the substitution and critical evaluation of analytical methods. *J. Mol. Struct.* **2005**, *744*, 221-8.

(8) Chatzipanagis, K.; Iafisco, M.; Roncal-Herrero, T.; Bilton, M.; Tampieri, A.; Kröger, R.; Delgado-López, J. M. Crystallization of citrate-stabilized amorphous calcium phosphate to nanocrystalline apatite: a surface-mediated transformation. *CrystEngComm* **2016**, *18*, 3170-3.

(9) Dorozhkin, S. V. Amorphous calcium (ortho)phosphates. *Acta Biomater.* **2010**, *6*, 4457-75.

(10) Wang, Y.; Chen, J.; Wei, K.; Zhang, S.; Wang, X. Surfactant-assisted synthesis of hydroxyapatite particles. *Mater. Lett.* **2006**, *60*, 3227-31.

(11) Jiang, S.; Jin, W.; Wang, Y.-N.; Pan, H.; Sun, Z.; Tang, R. Effect of the aggregation state of amorphous calcium phosphate on hydroxyapatite nucleation kinetics. *RSC Adv.* **2017**, *7*, 25497-503.

(12) Gafurov, M.; Biktagirov, T.; Yavkin, B.; Mamin, G.; Filippov, Y.; Klimashina, E.; Putlayev, V.; Orlinskii, S. Nitrogen-containing species in the structure of the synthesized nano-hydroxyapatite. *JETP Lett.* **2014**, *99*, 196-203.

(13) Uskoković, V. Disordering the disorder as the route to a higher order: incoherent crystallization of calcium phosphate through amorphous precursors. *Cryst. Growth Des*. **2019**, *19*, 4340-57.

(14) Vecstaudza, J.; Gasik, M.; Locs, J. Amorphous calcium phosphate materials: Formation, structure and thermal behaviour. *J. Eur Ceram Soc.* **2019**, *39,* 1642-9.

(15) Fleet, M. E.; Liu, X.; King, P. L. Accommodation of the carbonate ion in apatite: An FTIR and X-ray structure study of crystals synthesized at 2-4 GPa. *Am. Mineral.* **2004**, *89*, 1422-32.

(16) Pan, H.; Darvell, B. W. Effect of carbonate on hydroxyapatite solubility. *Cryst. Growth Des.* **2010**, *10*, 845-50.

(17) Tropp, J.; Blumenthal, N. C.; Waugh, J. S. Phosphorus NMR study of solid amorphous calcium phosphate. *J. Am. Chem. Soc*. **1983**, *105*, 22-6.

(18) Gras, P.; Baker, A.; Combes, C.; Rey, C.; Sarda, S.; Wright, A. J.; Smith, M. E.; Hanna, J. V.; Gervais, C.; Laurencin, D.; Bonhomme, C. From crystalline to amorphous calcium pyrophosphates: A solid state Nuclear Magnetic Resonance perspective. *Acta Biomater*. **2016**, *31*, 348-57.

(19) Pan, H.; Jiang, S.; Zhang, T.; Tang, R. In situ solution study of calcium phosphate crystallization kinetics. *Meth. Enzymol.* **2013**, *532*, 129-44.

(20) Shen, Z.; Tian, D.; Zhang, X.; Tang, L.; Su, M.; Zhang, L.; Li, Z.; Hu, S.; Hou, D. Mechanisms of biochar assisted immobilization of Pb^{2+} by bioapatite in aqueous solution. *Chemosphere* **2018**, *190*, 260-6.

(21) Liu, G.; Talley, J. W.; Na, C.; Larson, S. L.; Wolfe, L. G. Copper doping improves hydroxyapatite sorption for arsenate in simulated groundwaters. *Environ. Sci. Technol.* **2010**, *44*, 1366-72.

(22) Kim, J.; Sambudi, N. S.; Cho, K. Removal of Sr^{2+} using high-surface-area hydroxyapatite synthesized by non-additive in-situ precipitation. *J. Environ. Manage*. **2019**, *231*, 788-94.

(23) Ivanchenko, P.; Delgado-López, J. M.; Iafisco, M.; Gómez-Morales, J.; Tampieri, A.; Martra, G.; Sakhno, Y. On the surface effects of citrates on nano-apatites: evidence of a decreased hydrophilicity. *Sci. Rep.* **2017**, *7*, 8901.

(24) Cheng, S.; Wang, Z.; Sun, K.; Dong, J.; Li, X. Biomimetic fabrication of mulberry-like nano-hydroxyapatite with high specific surface area templated by dual-hydrophilic block copolymer. *Ceram. Int.* **2017**, *43*, 13430-7.

(25) Vecstaudza, J.; Locs, J. Novel preparation route of stable amorphous calcium phosphate nanoparticles with high specific surface area. *J. Alloys Compd.* **2017**, *700*, 215-22.

(26) Luginina, M.; Orru, R.; Cao, G.; Grossin, D.; Brouillet, F.; Chevallier, G.; Thouron, C.; Drouet, C., First successful stabilization of consolidated amorphous calcium phosphate (ACP) by cold sintering: toward highly-resorbable reactive bioceramics. *J Mater Chem B*. **2020**, 8 (4), 629-635.